© ESO 2017

Mapping the hot gas temperature in galaxy clusters using X-ray and Sunyaev-Zel'dovich imaging

R. Adam[1,2]*, M. Arnaud[3], I. Bartalucci[3], P. Ade[4], P. André[3], A. Beelen[5], A. Benoît[6], A. Bideaud[4], N. Billot[7], H. Bourdin[8], O. Bourrion[2], M. Calvo[6], A. Catalano[2], G. Coiffard[9], B. Comis[2], A. D'Addabbo[6,10], F.-X. Désert[11], S. Doyle[4], C. Ferrari[1], J. Goupy[6], C. Kramer[7], G. Lagache[12], S. Leclercq[9], J.-F. Macías-Pérez[2], S. Maurogordato[1], P. Mauskopf[4,13], F. Mayet[2], A. Monfardini[6], F. Pajot[5], E. Pascale[4], L. Perotto[2], G. Pisano[4], E. Pointecouteau[14,15], N. Ponthieu[11], G.W. Pratt[3], V. Revéret[3], A. Ritacco[2], L. Rodriguez[3], C. Romero[9], F. Ruppin[2], K. Schuster[9], A. Sievers[7], S. Triqueneaux[6], C. Tucker[4], and R. Zylka[9]

1. Laboratoire Lagrange, Université Côte d'Azur, Observatoire de la Côte d'Azur, CNRS, Blvd de l'Observatoire, CS 34229, 06304 Nice cedex 4, France
2. Laboratoire de Physique Subatomique et de Cosmologie, Université Grenoble Alpes, CNRS/IN2P3, 53, avenue des Martyrs, Grenoble, France
3. Laboratoire AIM, IRFU/Département d'Astrophysique - CEA/DRF - CNRS - Université Paris Diderot, Bât. 709, CEA-Saclay, F-91191 Gif-sur-Yvette Cedex, France
4. Astronomy Instrumentation Group, University of Cardiff, UK
5. Institut d'Astrophysique Spatiale (IAS), CNRS and Université Paris Sud, Orsay, France
6. Institut Néel, CNRS and Université Grenoble Alpes, France
7. Institut de RadioAstronomie Millimétrique (IRAM), Granada, Spain
8. Dipartimento di Fisica, Università degli Studi di Roma 'Tor Vergata', via della Ricerca Scientifica, 1, I-00133 Roma, Italy
9. Institut de RadioAstronomie Millimétrique (IRAM), Grenoble, France
10. Dipartimento di Fisica, Sapienza Università di Roma, Piazzale Aldo Moro 5, I-00185 Roma, Italy
11. Institut de Planétologie et d'Astrophysique de Grenoble (IPAG), CNRS and Université Grenoble Alpes, France
12. Aix Marseille Université, CNRS, LAM (Laboratoire d'Astrophysique de Marseille) UMR 7326, 13388, Marseille, France
13. School of Earth and Space Exploration and Department of Physics, Arizona State University, Tempe, AZ 85287
14. Université de Toulouse, UPS-OMP, Institut de Recherche en Astrophysique et Planétologie (IRAP), Toulouse, France
15. CNRS, IRAP, 9 Av. colonel Roche, BP 44346, F-31028 Toulouse cedex 4, France

Abstract

We propose a method to map the temperature distribution of the hot gas in galaxy clusters that uses resolved images of the thermal Sunyaev-Zel'dovich (tSZ) effect in combination with X-ray data. Application to images from the New IRAM KIDs Array (NIKA) and XMM-*Newton* allows us to measure and determine the spatial distribution of the gas temperature in the merging cluster MACS J0717.5+3745, at $z = 0.55$. Despite the complexity of the target object, we find a good morphological agreement between the temperature maps derived from X-ray spectroscopy only – using XMM-*Newton* (T_{XMM}) and *Chandra* (T_{CXO}) – and the new gas-mass-weighted tSZ+X-ray imaging method (T_{SZX}). We correlate the temperatures from tSZ+X-ray imaging and those from X-ray spectroscopy alone, finding that T_{SZX} is higher than T_{XMM} and lower than T_{CXO}, by $\sim 10\%$ in both cases. Our results are limited by uncertainties in the geometry of the cluster gas, contamination from kinetic SZ ($\sim 10\%$), and the absolute calibration of the tSZ map (7%). Investigation using a larger sample of clusters would help to minimise these effects.

1. Introduction

In galaxy clusters, the temperature and density are the key observable characteristics of the hot ionized gas in the intracluster medium (ICM). X-ray observations play a fundamental role in their measurement: the density is trivial to obtain from X-ray imaging, while the temperature can be derived from an isothermal model fit to the spectrum. Accurate gas temperatures are needed for a number of reasons. They are essential to infer cluster masses under the assumption of hydrostatic equilibrium (Sarazin 1988); in turn, these masses can be used to infer constraints on cosmological parameters (e.g., Allen et al. 2011). The tem-

perature structure yields information on the detailed physics of shock-heated gas in merging events, the nature of cold fronts, and the role of turbulence and gas sloshing (see, e.g., Markevitch & Vikhlinin 2007, for a review). In turn, such analyses provide insights into the assembly physics of galaxy clusters, which is necessary to interpret the scaling relations between clusters masses and their primary observables (Khedekar et al. 2013).

However, the X-ray gas temperature measurement is potentially affected by two systematic effects. First, the X-ray emission is proportional to the square of the ICM electron density, such that spectroscopic temperatures are driven by the colder, denser, regions along the line-of-sight, and are thus sensitive to gas clumping. What is measured is in fact a weighted mean temperature,

---

* Corresponding author: Rémi Adam, `remi.adam@oca.eu`

where the weight is a non-linear combination of the temperature and density structure (see, e.g., Mazzotta et al. 2004; Vikhlinin 2006). Numerical simulations support this view (e.g., Nagai et al. 2007; Rasia et al. 2014), but estimates of the magnitude of any bias due to this effect vary widely depending on the numerical scheme (e.g., smoothed particle hydrodynamics, adaptive mesh refinement) and the details of the 'sub-grid' physics (cooling, feedback, etc). Secondly, the spectroscopic temperatures depend directly on the energy calibration of X-ray observatories. For instance, X-ray temperatures obtained with *Chandra* are generally higher than those measured by XMM-*Newton*, by up to a factor of 15% at 10 keV (e.g., Mahdavi et al. 2013).

The thermal Sunyaev-Zel'dovich (tSZ, Sunyaev & Zeldovich 1972) effect is related to the mean gas-mass-weighted temperature along the line-of-sight and the electron density, via the ideal gas law. The tSZ effect can thus be used to obtain an alternative estimate of the gas temperature, provided a measure of the density is available. Combination of the tSZ and X-ray observations can then in principle be used to decouple temperature and density in each individual measurement. Such a method has previously been used to extract 1D gas temperature profiles, complementing X-ray spectroscopic measurements (e.g., Pointecouteau et al. 2002; Kitayama et al. 2004; Nord et al. 2009; Basu et al. 2010; Eckert et al. 2013; Ruppin et al. 2017).

Here, we explore the application of the method to two dimensional data. We use deep, resolved ($< 20''$) tSZ observations, combined with X-ray imaging, to measure the spatial distribution of the gas temperature toward the merging cluster MACS J0717.5+3745 at $z = 0.55$. We have chosen MACS J0717.5+3745 as a test case cluster because it is one of the very few objects for which tSZ data of sufficient depth and resolution are currently available (Adam et al. 2017). The complex morphology of the cluster is the primary limiting factor to our analysis; however the system allows us to explore a wide range of gas temperatures, which will not necessarily be accessible with more simple objects. We compare our new temperature map, based on X-ray and tSZ imaging, to that obtained from application of standard X-ray spectroscopic techniques using XMM-*Newton* and *Chandra* data. We describe and discuss in detail the various factors affecting the ratio between the two temperature estimates.

We assume a flat ΛCDM cosmology according to the latest *Planck* results (Planck Collaboration et al. 2015) with $H_0 = 67.8$ km s^{-1} Mpc^{-1}, $\Omega_M = 0.308$, and $\Omega_\Lambda = 0.692$. At the cluster redshift, 1 arcsec corresponds to 6.6 kpc.

2. Data

The New IRAM KIDs Array (NIKA, see Monfardini et al. 2011; Calvo et al. 2013; Adam et al. 2014; Catalano et al. 2014) has observed MACS J0717.5+3745 at 150 and 260 GHz for a total of 47.2 ks. The main steps of the data reduction are described in Adam et al. (2015, 2016, 2017); Ruppin et al. (2017). In this paper, we use the NIKA 150 GHz tSZ map at 22 arcsec effective angular resolution FWHM, deconvolved from the transfer function except for the beam smoothing. The overall calibration uncertainty is estimated to be 7%, including the brightness temperature model of our primary calibrator, the NIKA bandpass uncertainties, the opacity correction, and the stability of the instrument (Catalano et al. 2014). The absolute zero level for the brightness on the map remains unconstrained by NIKA. MACS J0717.5+3745 is contaminated by a significant amount of kinetic SZ (kSZ, Sunyaev & Zeldovich 1980) signal and we used the best-fit model F2 from Adam et al. (2017) to remove its contribution. This model has

large uncertainties but it still allows us to test the impact of the kSZ effect on our results.

MACS J0717.5+3745 was observed several times by the XMM-*Newton* and *Chandra* X-ray observatories (obs-IDs 0672420101, 0672420201, 067242030, and 1655, 4200, 16235, 16305, respectively). The data processing follows the description given in Adam et al. (2017). The clean exposure time is 153 ks for *Chandra* and 160 and 116 ks for XMM-*Newton* MOS1,2 and PN cameras, respectively.

3. Temperature reconstruction

The method employed to recover the temperature of the gas from NIKA tSZ and XMM-*Newton* X-ray imaging, T_{SZX}, is described below. The X-ray spectroscopic temperature mapping method is discussed in Section 3.6 and Appendix A.

3.1. Primary observables

The tSZ signal, measured at frequency ν, can be expressed as

$$\frac{\Delta I_\nu}{I_0} = f(\nu, T_e) \frac{\sigma_{\mathrm{T}}}{m_e c^2} \int P_e \, dl \equiv k_{\mathrm{B}} T_{\mathrm{gmw}} f(\nu, T_e) \frac{\sigma_{\mathrm{T}}}{m_e c^2} \int n_e dl,$$
(1)

where $f(\nu, T_e)$ is the tSZ spectrum, which depends slightly on temperature T_e in the case of very hot gas. The signal is proportional to the line-of-sight integrated electron pressure, P_e. It is related to the mean gas-mass-weighted temperature along the line-of-sight,

$$T_{\mathrm{gmw}} \equiv \frac{\int T_e n_e dl}{\int n_e dl},$$
(2)

and the electron density, n_e, via the ideal gas law. The X-ray surface brightness is driven by the electron density:

$$S_{\mathrm{X}} = \frac{1}{4\pi (1+z)^4} \int n_e^2 \Lambda(T_e, Z) \, dl,$$
(3)

where z is the cluster redshift, and $\Lambda(T_e, Z)$ is the emissivity in the relevant energy band, taking into account the interstellar absorption and the instrument spectral response. $\Lambda(T_e, Z)$ depends only weakly on the temperature and metallicity of the gas Z, so that instrumental systematics have a negligible impact on the results presented in this paper.

3.2. X-ray electron density mapping

We use the XMM-*Newton* X-ray surface brightness (equation 3) to produce a map of the square of the electron density integrated along the line-of-sight, $\int n_e^2 dl$. To combine it with tSZ observations, we have to convert $\int n_e^2 dl$ to $\int n_e dl$ via an effective electron depth, expressed as

$$\ell_{\mathrm{eff}} = \frac{\left(\int n_e dl\right)^2}{\int n_e^2 dl}.$$
(4)

From equation 3, the average density along the line-of-sight is then given by:

$$\overline{n}_e = \frac{1}{\ell_{\mathrm{eff}}} \int n_e dl = \frac{1}{\sqrt{l_{\mathrm{eff}}}} \sqrt{\frac{4\pi (1+z)^4 S_{\mathrm{X}}}{\Lambda(T_e, Z)}}.$$
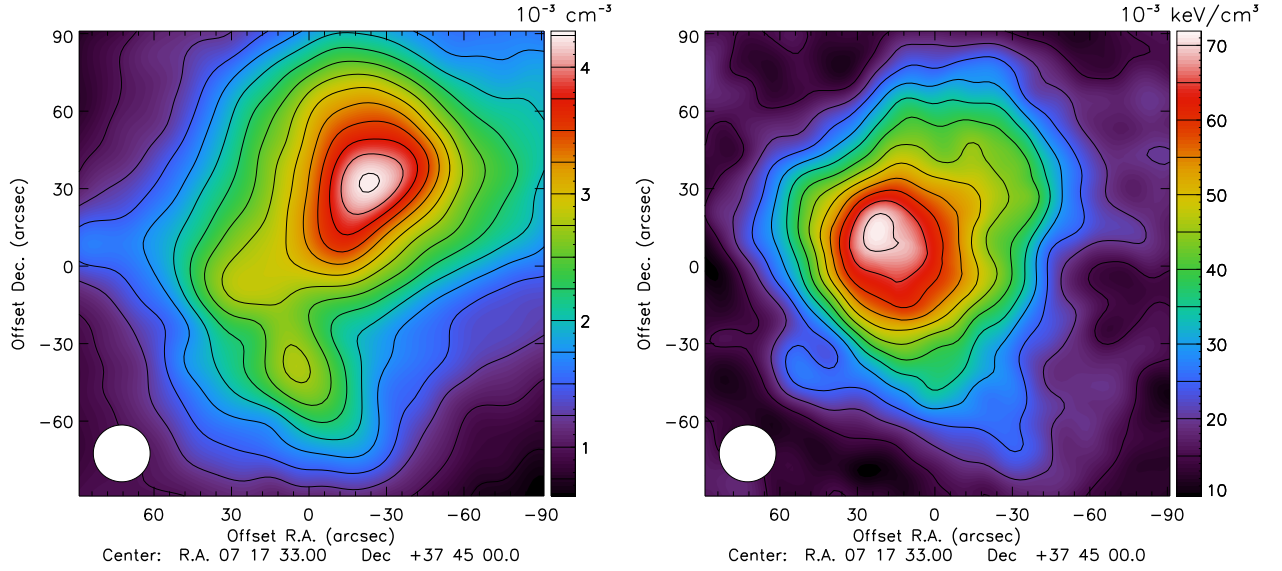(5)

defining an effective density.

Figure 1. Left: Effective line-of-sight electron density, $\overline{n}_e$, derived from XMM-*Newton*. **Right**: Effective line-of-sight pressure, $\overline{P}_e$, derived from NIKA. These maps correspond to model M1, and were smoothed with a Gaussian kernel to an effective resolution of 22 arcsec FWHM. The pressure map is cleaned from our best-fit kSZ model and corrected for the zero level.

3.3. Thermal Sunyaev-Zel'dovich pressure mapping

Similarly, we can express the effective pressure along the line-of-sight directly from equation 1, as

$$\overline{P}_e = \frac{1}{\ell_{\mathrm{eff}}} \int P_e dl = \frac{m_e c^2}{\sigma_T} \frac{y_{\mathrm{tSZ}}}{\ell_{\mathrm{eff}}}. \qquad (6)$$

This quantity is straightforwardly obtained from the NIKA map accounting for relativistic corrections as detailed in Adam et al. (2017). As the temperature can be very high, the relativistic corrections are non negligible (Pointecouteau et al. 1998; Itoh & Nozawa 2003), but the exact choice of the temperature map used to apply relativistic corrections has a negligible impact on our results (i.e., the spectroscopic temperature maps from XMM-*Newton*, from *Chandra*, or T_{SZX}).

3.4. Gas-mass-weighted temperature mapping

The tSZ+X-ray imaging temperature map, T_{SZX}, is obtained by combining the effective density and pressure:

$$k_B T_{\mathrm{SZX}} = \frac{\overline{P}_e}{\overline{n}_e} = \frac{1}{\sqrt{\ell_{\mathrm{eff}}}} \frac{m_e c^2}{\sigma_T} \sqrt{\frac{\Lambda\left(T_e, Z\right)}{4\pi\left(1+z\right)^4 S_X}} y_{\mathrm{tSZ}}. \qquad (7)$$

T_{SZX} is an estimate of the gas-mass-weighted temperature, T_{gmw} (equation 2). We propagate the noise arising from the tSZ map and the X-ray surface brightness using Monte Carlo realisations; the overall noise on T_{SZX} is dominated by that of the tSZ map. The sources of systematic errors are incorrect modeling of ℓ_{eff}, as well as tSZ calibration uncertainties and contamination from the kSZ effect. The absolute calibration error of the X-ray flux is expected to be negligible.

3.5. Effective electron depth

The effective electron depth is a key quantity for the method, as the derived gas-mass-weighted temperature scales with $\sqrt{\ell_{\mathrm{eff}}}$. It

can be re-expressed as

$$\ell_{\mathrm{eff}} = \frac{R_{500}}{Q_{n_e}^2} \quad \text{with} \quad Q_{n_e} = \frac{\sqrt{\langle n_e^2 \rangle}}{\langle n_e \rangle}, \qquad (8)$$

where the brackets denote averaging along the line-of-sight, done in scaled coordinates. The electron depth at each projected position depends, via the shape factor Q_{n_e}, on the geometry of the gas density distribution at all scales, from the large-scale radial dependence to small-scale fluctuations. In particular, Q_{n_e} increases with increasing gas concentration and clumpiness.

In the following, we use several approaches to estimate ℓ_{eff} and its uncertainty:

1. **Model M1:** Following Sayers et al. (2013), we assume that ℓ_{eff} is constant at $\ell_{\mathrm{eff}} = 1400$ kpc, as estimated by Mroczkowski et al. (2012), across the cluster extension.

2. **Model M2:** We derive an electron density profile from deconvolution and deprojection of the XMM-*Newton* radial S_X profile centered on the X-ray peak (Croston et al. 2006), thus obtaining an azimuthally symmetric ℓ_{eff} map.

3. **Model M3:** We use the best fitting NIKA tSZ+XMM-*Newton* density model of Adam et al. (2017), which accounts for the four main subclusters in MACS J0717.5+3745, to compute a map of ℓ_{eff}. The model does not constrain the line-of-sight distance between the subclusters because the tSZ signal depends linearly on the density. Therefore, we consider two extreme cases: **M3a)** where the subclusters are sufficiently far away from each other such that $\int n_e^2 dl \simeq \sum_j \int n_{e,j}^2 dl$, where j refers to each subcluster; **M3b)** where all the subclusters are located in the same plane, perpendicular to the line-of-sight. The physical distances between the subclusters are thus minimal, maximizing the $\int n_e^2 dl$ integral.

While the internal structure of MACS J0717.5+3745 is increasingly refined from model M1 to M3, we find good consistency between all three models. Model M2 presents a minimum of 1200 kpc toward the X-ray center and increases quasi-linearly toward higher radii, reaching about 2000 kpc at 1 arcmin, in line with expectations from model M1. Model M3a is minimal in the
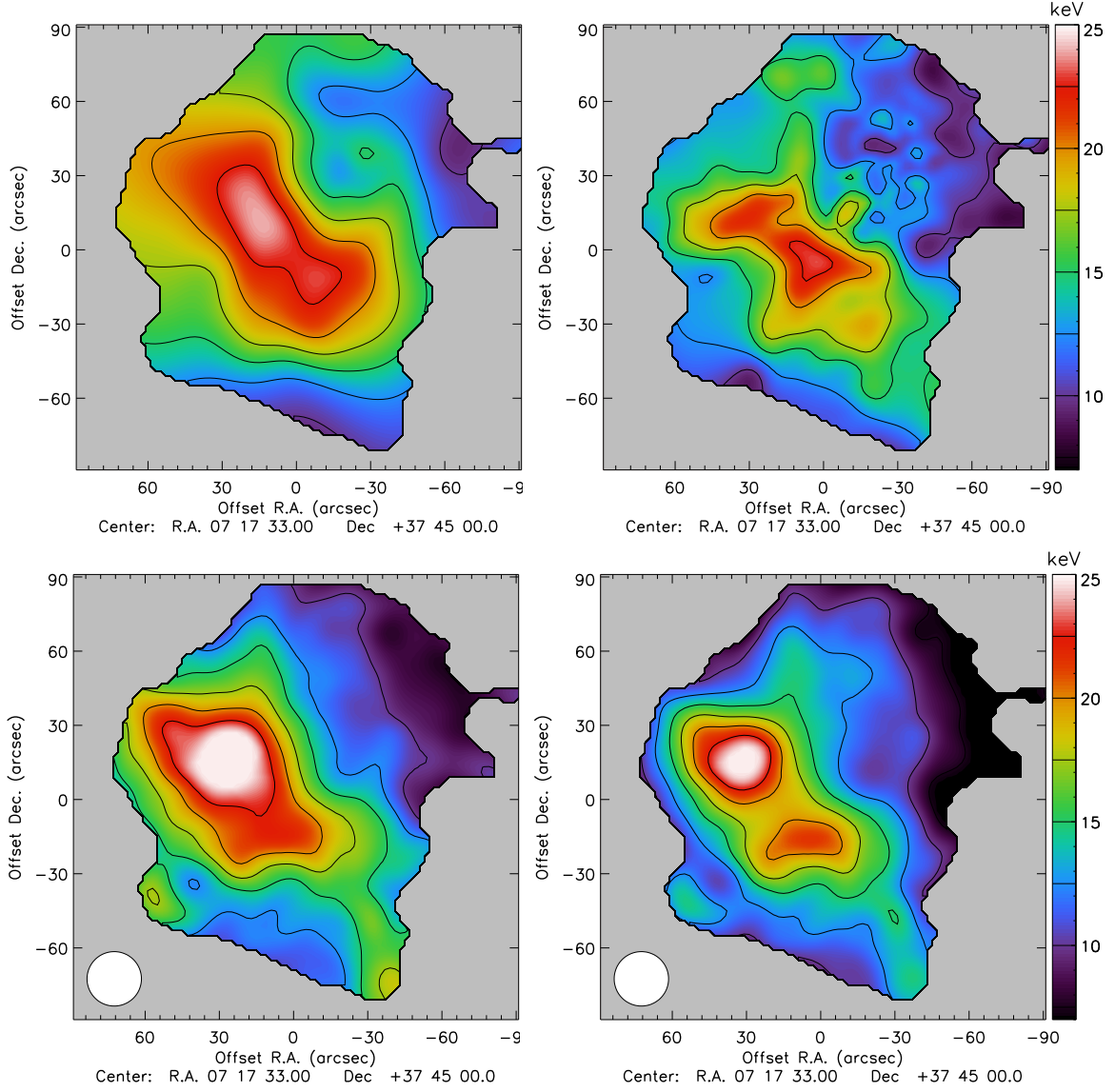
Figure 2. Temperature maps. **Top**: Spectroscopic temperature derived from *Chandra* ($T_{\rm CXO}$, left panel) and from XMM-*Newton* ($T_{\rm XMM}$, right panel). **Bottom**: NIKA+XMM-*Newton* imaging derived temperature, $T_{\rm SZX}$, for model M1 (left panel) and model M3a (right panel). These maps are corrected for the zero level.

central region, in the direction of the subclusters (~ 1200 kpc), and also increases with radius. Model M3b provides a lower limit for $\ell_{\rm eff}$, increasing from ~ 800 kpc near the center to ~ 1200 kpc at 1 arcmin.

While these models allow us to test the impact of the gas geometry on large scales, they do not specifically account for clumping on small scales. Despite the weak dependence of the gas-mass-weighted temperature on the electron depth ($\propto \sqrt{\ell_{\rm eff}}$), clumping might affect our results. We discuss this further in Section 4.

3.6. X-ray spectroscopic temperature maps

The X-ray spectroscopic temperature maps from *Chandra* ($T_{\rm CXO}$) and XMM-*Newton* ($T_{\rm XMM}$) were produced using the wavelet filtering algorithm described in Bourdin & Mazzotta (2008), as detailed in Adam et al. (2017). As the significance of wavelet coefficients partly depends on the photon count statistics, the effective resolution varies across the map, XMM-*Newton* allowing

a finer sampling than *Chandra* due to the higher effective area. We estimate the uncertainties per map pixel using a Monte Carlo approach, as discussed in Appendix A.

Comparison of the temperature derived from tSZ and X-ray imaging to the X-ray spectroscopic temperature provides further information on the ICM structure, and also on calibration systematics. From equations 7 and 8, at each projected position, the ratio of the two temperatures can be expressed as

$$\frac{T_{\rm SZX}}{T_{\rm X}} = \frac{T_{\rm gmw}}{T_{\rm spec}} \frac{Q_{n_{\rm e}, \, \rm model}}{Q_{n_{\rm e}, \, \rm true}} C_{\rm X} \, C_{\rm SZ}, \qquad (9)$$

where $T_{\rm gmw}$ is the 'true' gas-mass-weighted temperature and $T_{\rm spec}$ is the spectroscopic temperature that would be obtained by fitting an isothermal model to the observed spectra for a perfectly calibrated instrument. $C_{\rm X} = T_{\rm spec}/T_{\rm X}$ is the ratio between the latter and the measured X-ray temperature, which accounts for the X-ray calibration uncertainty. $C_{\rm SZ}$ accounts for the tSZ calibration.

The measured ratio $T_{\rm SZX}/T_{\rm X}$ is an estimate of the ratio between the gas-mass-weighted temperature and the spectroscopic
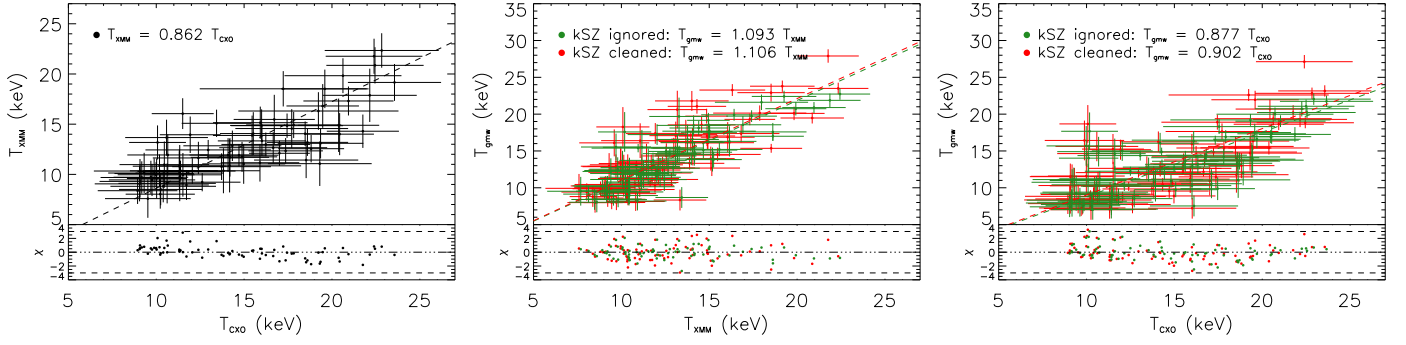
Figure 3. Correlation between the temperature maps of Figure 2 and residual. **Left:** XMM-*Newton* versus *Chandra* spectroscopic temperatures. **Middle:** tSZ+X-ray imaging (model M1) versus XMM-*Newton* spectroscopy. **Right:** tSZ+X-ray imaging (model M1) versus *Chandra* spectroscopy. The red and green dots correspond to the case with and without the kSZ correction, respectively.

temperature, $Q_T = T_{\rm gmw}/T_{\rm spec}$. $T_{\rm spec}$ is expected to be biased low as compared to the gas-mass-weighted temperature and depends on the instrument used to make the measurement. The ratio Q_T is a shape parameter, which depends on both the density and the temperature structure along the line-of-sight. In addition to calibration issues, the measured ratio $T_{\rm SZX}/T_X$ may differ from Q_T if the density shape factor, Q_{n_e}, is incorrect. For a given cluster, the various terms on the right hand side of equation 9 are in principle degenerate. Part of the degeneracy, in particular of 'calibration' versus physical factors, can be broken by taking into account the expected differences in spatial dependence.

4. Results

4.1. Morphology

The left panel and right panel of Figure 1 represent the effective density and pressure maps in the case of the simplest model M1, thus $\propto \sqrt{\int n_e^2 dl}$ and $\propto \int P_e dl$, respectively. The pressure map is corrected for the kSZ and the zero level (see Section 4.2). The cluster clearly exhibits a disturbed morphology. The morphology of the ICM pressure is similar to that of the density on large scales, but we observe strong differences at the substructure level, indicating spatial variations of the temperature. We note in particular that the pressure peak is offset ~ 30 arcsec southeast with respect to the density peak.

Figure 2 shows the temperature maps $T_{\rm CXO}$, $T_{\rm XMM}$, and $T_{\rm SZX}$ for models M1 and M3a. $T_{\rm SZX}$ is corrected for the zero level and kSZ-corrected. All the maps identify a hot gas 'bar' to the southeast. The position of the temperature peak is the same for $T_{\rm CXO}$ and $T_{\rm SZX}$, while it is slightly shifted southwest for $T_{\rm XMM}$; however it also coincides with a region where kSZ contamination is large, leading to possible overestimation in $T_{\rm SZX}$. All four maps indicate cooler temperatures in the the northwest sector. Varying the kSZ correction and the $\ell_{\rm eff}$ models changes slightly the local morphology of $T_{\rm SZX}$ in the 'bar'. Use of model M3a leads to the appearance of a secondary peak, while there is also a hint of a bimodal bar structure in the X-ray spectroscopic maps. However, the general agreement with the X-ray spectroscopic results, both in terms of absolute temperature and morphology, is good in all cases.

4.2. Temperature comparison

Figure 3 shows the correlation between the maps shown in Figure 2. Both tSZ and X-ray temperature values were extracted in 20

arcsec pixels (see Appendix B for details). We masked pixels where the tSZ signal-to-noise ratio SNR < 2 to avoid possible bouncing effects on the edge of the map due to the NIKA data processing.

Since the zero level of the tSZ map is unconstrained, we express the effective pressure map as $\overline{P}_e = \overline{P}_{\rm true} + \overline{P}_0$, where $\overline{P}_0$ is an unknown offset. Following equation 7, the gas-mass-weighted temperature can then be expressed with respect to the spectroscopic temperature as

$$k_B T_{\rm SZX} = \alpha_{\rm SZX} \times k_B T_{\rm XMM/CXO} + \beta/\overline{n}_e, \qquad (10)$$

where β gives a measurement of $\overline{P}_0$. For X-ray spectroscopic temperatures, we simply write $T_{\rm XMM} = \alpha_{\rm XMM-CXO} \times T_{\rm CXO}$. We perform a linear regression between the pairs of temperature maps accounting for error bars on both axis, as detailed in Appendix B. Table 1 gives the α and β coefficients and the intrinsic scatter, obtained for the different $\ell_{\rm eff}$ models tested, and their dependence on the kSZ correction. Figure 4 provides the posterior likelihood in the $\alpha_{\rm SZX} - \beta$ plane for all the regressions performed between $T_{\rm SZX}$ and $T_{\rm XMM/CXO}$.

The ratio of the temperature obtained from tSZ+X-ray imaging versus the temperature obtained from X-ray spectroscopy is stable to within 10%, depending on the choice of the $\ell_{\rm eff}$ model and the kSZ correction used. Model M3b provides a lower limit on $\ell_{\rm eff}$, and therefore an upper limit on $\alpha_{\rm SZX}$. The scatter of about 2 keV between $T_{\rm CXO}$ and $T_{\rm XMM}$ is dominated by the statistical error. The scatter between $T_{\rm SZX}$ and both X-ray temperatures are comparable, but slightly lower for $T_{\rm XMM}$. In most cases, the scatter is compatible with the noise as propagated into the $T_{\rm SZX}$ and T_X maps. The intrinsic scatter is only detected significantly, at the $\sim 2 - 3\sigma$ level, for the model M3a. This may be due to a number of factors, including the difference in angular resolution of the maps, or an intrinsic scatter between gas-mass-weighted and spectroscopic temperatures.

Figure 3 and Table 1 indicate that *Chandra* temperatures are about 15% higher than those of XMM-*Newton*, as found by previous work (Mahdavi et al. 2013; Schellenberger et al. 2015), while $T_{\rm SZX}$ is on average larger than $T_{\rm XMM}$ and lower than $T_{\rm CXO}$ by about 10%. The reasonable agreement between $T_{\rm SZX}$ and T_X suggests that there is no major flaw in the method and/or unidentified systematic effects in the analysis.

When dealing with multiphase plasma, X-ray spectroscopic temperatures are expected to underestimate the gas temperature by 10-20% (Mathiesen & Evrard 2001; Mazzotta et al. 2004). This is particularly important in the presence of strong temperature gradients, as would be expected in strong mergers such as
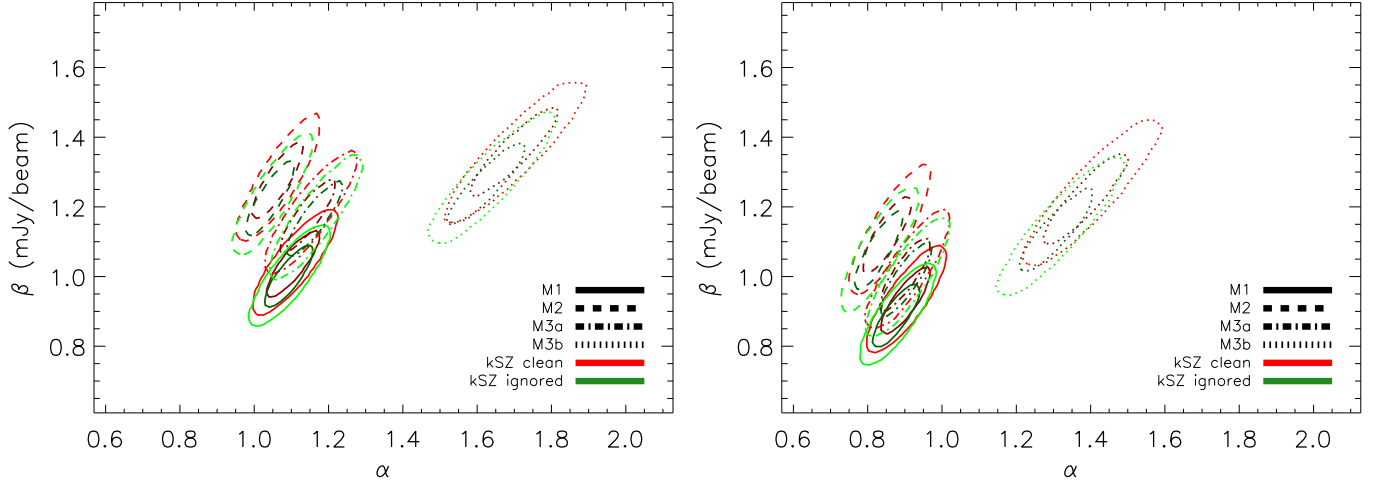
Figure 4. Posterior likelihood (68 and 95% C.L.) in the plane $\alpha - \beta$ (expressed in term of the zero level brightness of the NIKA map). **Left:** tSZ+X-ray imaging versus XMM-*Newton* spectroscopy. **Right:** tSZ+X-ray imaging versus *Chandra* spectroscopy. The red and green dots correspond to the case with and without the kSZ correction, respectively and the different models are provided with different dashed line as shown in the legend.

Table 1. Regression and intrinsic scatter coefficients between the temperature maps. The central value is the median of the posterior likelihood and the errors are obtained by integrating the posterior likelihood within 90% C.L. The posterior likelihood distribution is highly non Gaussian in the case of the scatter and error bars should be interpreted with caution. *Model M3b gives a lower limit for ℓ_{eff}, and thus should be taken only as an upper limit for α.

Slope / offset (mJy/Beam) / scatter (keV)	ℓ_{eff} model			
	M1	M2	M3a	M3b*
	kSZ-corrected			
$(\alpha, \beta, \sigma_{\mathrm{int}})_{\mathrm{SZX-XMM}}$	$(1.11^{+0.08}_{-0.07}, 1.04^{+0.10}_{-0.10}, 1.43^{+0.38}_{-0.62})$	$(1.06^{+0.07}_{-0.07}, 1.28^{+0.12}_{-0.12}, 1.29^{+0.35}_{-0.60})$	$(1.15^{+0.08}_{-0.08}, 1.17^{+0.12}_{-0.11}, 1.59^{+0.37}_{-0.55})$	$(1.70^{+0.13}_{-0.12}, 1.36^{+0.14}_{-0.14}, 2.44^{+0.50}_{-0.71})$
$(\alpha, \beta, \sigma_{\mathrm{int}})_{\mathrm{SZX-CXO}}$	$(0.90^{+0.07}_{-0.07}, 0.93^{+0.11}_{-0.10}, 1.59^{+0.47}_{-0.78})$	$(0.85^{+0.07}_{-0.06}, 1.12^{+0.13}_{-0.12}, 1.51^{+0.41}_{-0.67})$	$(0.90^{+0.08}_{-0.07}, 1.01^{+0.12}_{-0.11}, 2.51^{+0.36}_{-0.40})$	$(1.39^{+0.14}_{-0.11}, 1.23^{+0.16}_{-0.13}, 2.50^{+0.64}_{-1.00})$
	kSZ-uncorrected			
$(\alpha, \beta, \sigma_{\mathrm{int}})_{\mathrm{SZX-XMM}}$	$(1.09^{+0.07}_{-0.07}, 1.00^{+0.10}_{-0.09}, 0.00^{+0.56}_{-0.00})$	$(1.04^{+0.07}_{-0.07}, 1.23^{+0.12}_{-0.11}, 0.00^{+0.61}_{-0.00})$	$(1.16^{+0.08}_{-0.08}, 1.17^{+0.12}_{-0.11}, 1.51^{+0.37}_{-0.61})$	$(1.63^{+0.12}_{-0.11}, 1.27^{+0.13}_{-0.13}, 0.00^{+0.69}_{-0.00})$
$(\alpha, \beta, \sigma_{\mathrm{int}})_{\mathrm{SZX-CXO}}$	$(0.88^{+0.07}_{-0.06}, 0.89^{+0.10}_{-0.09}, 0.73^{+0.71}_{-0.73})$	$(0.83^{+0.07}_{-0.06}, 1.08^{+0.12}_{-0.12}, 0.82^{+0.60}_{-0.82})$	$(0.90^{+0.08}_{-0.07}, 1.00^{+0.12}_{-0.11}, 2.52^{+0.35}_{-0.40})$	$(1.31^{+0.12}_{-0.10}, 1.13^{+0.14}_{-0.13}, 0.60^{+1.25}_{-0.60})$
$(\alpha, \sigma_{\mathrm{int}})_{\mathrm{XMM-CXO}}$	$(0.86^{+0.03}_{-0.03}, 0.00^{+0.00}_{-0.00})$			

MACS J0717.5+3745. We observe such a difference when comparing T_{SZX} with the lower T_{XMM} values, but not with T_{CXO}. This must not be over-interpreted in terms of X-ray calibration. First, the difference is not very significant, taking into account the statistical errors on the ratio ($\sim 7\%$, Table 1) and the absolute calibration of the tSZ map, which is expected to be accurate to within 7%. Furthermore, the gas clumpiness is not taken into account in the model. This would under-estimate the Q_{n_e} factor and thus the measured T_{SZX} values (equation 9). For instance, combining Planck tSZ (Planck Collaboration et al. 2016) and XMM-*Newton* observations, Tchernin et al. (2016) find the Q_{n_e} clumpiness factor to be about 10% in the cluster Abell 2142 within 1 Mpc from the centre, increasing to about 20% at R_{200}. Numerical simulations suggest a factor of up to $\sim 40\%$ at R_{200}, but with a rather large cluster-to-cluster scatter (e.g., Nagai & Lau 2011; Zhuravleva et al. 2013; Vazza et al. 2013). A clumpiness factor of 20% would put T_{SZX} in better agreement with T_{CXO} values. This illustrates the difficulty to disentangle various instrumental effects and intrinsic cluster properties, especially on a single cluster with a particularly complex morphology.

5. Conclusions

Using deep tSZ observations together with X-ray imaging, we have extracted an ICM temperature map of the galaxy cluster MACS J0717.5+3745. This map is gas-mass-weighted and provides an alternative to purely X-ray spectroscopic based methods. The test cluster being extremely hot, with the peak temperature reaching up to ~ 25 keV, allows us to sample a large range of temperature, which would not be accessible with the large majority of clusters.

The morphological comparison of the gas-mass-weighted temperature map to XMM-*Newton* and *Chandra* X-ray spectroscopic maps indicates good agreement between the different methods. All three maps are consistent with MACS J0717.5+3745 having a low-temperature in the northwest region and presenting a bar-like high temperature structure to the southeast, indicative of heating from adiabatic compression owing to the merger between two main subclusters (see, e.g., Ma et al. 2009).

We performed a first quantitative comparison between the various maps. The ratio of the temperature obtained from tSZ+X-ray imaging versus the temperature obtained from X-ray spectroscopy is stable to within 10%, depending on the choice of the large scale density model and the kSZ correction used. We found that *Chandra* temperatures are about 15% higher than those of XMM-*Newton*, as found by previous work, while T_{SZX} is on average higher than T_{XMM} and lower than T_{CXO} by about 10% in each case. Such ratios are typical and are consistent with expectations, taking into account cluster structures and measurement systematics. The gas-mass-weighted temperature map we have derived is limited by the complexity of the test cluster and by assumptions on the effective electron depth of the ICM, kSZ contamination, and the calibration of the NIKA instrument. For a perfectly spherical cluster, the ratio $T_{\mathrm{X}}/T_{\mathrm{SZX}}$ would give access to absolute calibration of the X-ray temperature. Clusters being complex objects, the ratio we really measure is a complicated

combination of the 3D temperature structure and intrinsic properties affecting the density such as amount of substructure, gas clumpiness and triaxiality. A larger sample would allow us to disentangle instrumental calibration from effects linked to intrinsic cluster properties.

We note that the noise in our T_{SZX} map is significantly lower, especially at high temperatures, to that obtained from XMM-*Newton* and *Chandra*, but obtained with a factor of three smaller observing time. This illustrates the potential of resolved tSZ observations at intermediate to high redshifts, where X-ray spectroscopy becomes challenging, and which should be routinely provided by the up-coming generation of SZ instruments, MUSTANG2 (Dicker et al. 2014) and NIKA2 (Calvo et al. 2016; Comis et al. 2016).

References

Adam, R. et al. 2017, A&A, 598, A115, 1606.07721
——. 2016, A&A, 586, A122, 1510.06674
——. 2015, A&A, 576, A12, 1410.2808
——. 2014, A&A, 569, A66, 1310.6237
Allen, S. W., Evrard, A. E., & Mantz, A. B. 2011, ARA&A, 49, 409, 1103.4829
Basu, K. et al. 2010, A&A, 519, A29, 0911.3905
Bourdin, H., & Mazzotta, P. 2008, A&A, 479, 307, 0802.1866
Calvo, M. et al. 2016, Journal of Low Temperature Physics, 1601.02774
——. 2013, A&A, 551, L12
Catalano, A. et al. 2014, A&A, 569, A9, 1402.0260
Chib, S., & Greenberg, E. 1995, The American Statistician, 49, 327
Comis, B. et al. 2016, ArXiv e-prints, 1605.09549
Croston, J. H., Arnaud, M., Pointecouteau, E., & Pratt, G. W. 2006, A&A, 459, 1007, astro-ph/0608700
Dicker, S. R. et al. 2014, in Proc. SPIE, Vol. 9153, Millimeter, Submillimeter, and Far-Infrared Detectors and Instrumentation for Astronomy VII, 91530J
Eckert, D., Molendi, S., Vazza, F., Ettori, S., & Paltani, S. 2013, A&A, 551, A22, 1301.0617
Itoh, N., & Nozawa, S. 2003, ArXiv Astrophysics e-prints, astro-ph/0307519
Khedekar, S., Churazov, E., Kravtsov, A., Zhuravleva, I., Lau, E. T., Nagai, D., & Sunyaev, R. 2013, MNRAS, 431, 954, 1211.3358
Kitayama, T., Komatsu, E., Ota, N., Kuwabara, T., Suto, Y., Yoshikawa, K., Hattori, M., & Matsuo, H. 2004, PASJ, 56, 17, astro-ph/0311574
Ma, C.-J., Ebeling, H., & Barrett, E. 2009, ApJ, 693, L56, 0901.4783
Mahdavi, A., Hoekstra, H., Babul, A., Bildfell, C., Jeltema, T., & Henry, J. P. 2013, ApJ, 767, 116, 1210.3689
Markevitch, M., & Vikhlinin, A. 2007, Phys. Rep., 443, 1, astro-ph/0701821
Mathiesen, B. F., & Evrard, A. E. 2001, ApJ, 546, 100, astro-ph/0004309
Mazzotta, P., Rasia, E., Moscardini, L., & Tormen, G. 2004, MNRAS, 354, 10, astro-ph/0404425
Monfardini, A. et al. 2011, ApJS, 194, 24, 1102.0870
Mroczkowski, T. et al. 2012, ApJ, 761, 47, 1205.0052
Nagai, D., & Lau, E. T. 2011, ApJ, 731, L10, 1103.0280
Nagai, D., Vikhlinin, A., & Kravtsov, A. V. 2007, ApJ, 655, 98, astro-ph/0609247
Nord, M. et al. 2009, A&A, 506, 623, 0902.2131
Orear, J. 1982, American Journal of Physics, 50, 912
Planck Collaboration et al. 2016, A&A, 594, A1, 1502.01582
——. 2015, ArXiv e-prints, 1502.01589

Pointecouteau, E., Giard, M., & Barret, D. 1998, A&A, 336, 44, astro-ph/9712271
Pointecouteau, E., Hattori, M., Neumann, D., Komatsu, E., Matsuo, H., Kuno, N., & Böhringer, H. 2002, A&A, 387, 56, astro-ph/0203268
Pratt, G. W., Croston, J. H., Arnaud, M., & Böhringer, H. 2009, A&A, 498, 361, 0809.3784
Rasia, E. et al. 2014, ApJ, 791, 96
Ruppin, F. et al. 2017, A&A, 597, A110, 1607.07679
Sarazin, C. L. 1988, X-ray emission from clusters of galaxies
Sayers, J. et al. 2013, ApJ, 778, 52, 1312.3680
Schellenberger, G., Reiprich, T. H., Lovisari, L., Nevalainen, J., & David, L. 2015, A&A, 575, A30, 1404.7130
Sunyaev, R. A., & Zeldovich, I. B. 1980, MNRAS, 190, 413
Sunyaev, R. A., & Zeldovich, Y. B. 1972, Comments on Astrophysics and Space Physics, 4, 173
Tchernin, C. et al. 2016, A&A, 595, A42, 1606.05657
Vazza, F., Eckert, D., Simionescu, A., Brüggen, M., & Ettori, S. 2013, MNRAS, 429, 799, 1211.1695
Vikhlinin, A. 2006, ApJ, 640, 710, astro-ph/0504098
Zhuravleva, I., Churazov, E., Kravtsov, A., Lau, E. T., Nagai, D., & Sunyaev, R. 2013, MNRAS, 428, 3274, 1210.6706

Appendix A: X-ray spectroscopic temperature map error estimation

The X-ray spectroscopic temperature maps from *Chandra* (T_{CXO}) and XMM-*Newton* (T_{XMM}) were produced using the wavelet filtering algorithm described in Bourdin & Mazzotta (2008). Full details of its application to the present observations can be found in Adam et al. (2017). As the significance of wavelet coefficients partly depends on the photon count statistics, the effective resolution varies across the map, with the higher effective area of XMM-*Newton* allowing a finer sampling than *Chandra* due to its larger effective area. The pixels of the resulting maps are highly correlated, due to the nature of the algorithm, which combines different scales. For this reason, we estimate the uncertainties per map using a Monte Carlo approach.

In the algorithm developed by Bourdin & Mazzotta (2008), the X-ray photons are arranged in a 3D 'event cube' (j, k, e) where (j, k) are the sky coordinates and e is the energy. We generated mock observation event cubes for both XMM-*Newton* and *Chandra* where the energy coordinate e of each pixel was modelled by the spectrum of the best-fitting temperature from the maps described in Sect. 4. The appropriate response function, Galactic absorption value, and redshift were folded in during this procedure. Each model spectrum was normalised to match the surface brightness in each pixel, estimated producing a wavelet cleaned, background subtracted and exposure corrected image in the $[0.3 - 2.5]$ keV band.

We obtained a Monte Carlo realisation of the spectrum in each pixel to produce a new mock observation event cube. We then applied the same background subtraction procedure and wavelet filtering algorithm to this mock observation event cube, producing a new, randomised temperature map in the same way as for the real data. We did this 100 times, and took the range encompassing 68% of the Monte Carlo realisations as the uncertainty in the temperature map.

Appendix B: Correlation between the temperature maps

We performed a linear regression between the pairs of temperature maps ($\overline{T}_{1,2} \equiv T_{\mathrm{XMM}}, T_{\mathrm{CXO}}, T_{\mathrm{SZX}}$), accounting for error bars on both axis. The fit is linear, but the model is not a straight line due to the zero level dependance on the effective density map

(equation 10). To perform the fit, we followed Orear (1982) and defined the following likelihood, $\mathcal{L}$:

$$2 \ln \mathcal{L} = \sum_{i=1}^{N_{\mathrm{pix}}} \frac{\left(k_{\mathrm{B}} \overline{T}_1^{(i)} - \alpha\, k_{\mathrm{B}} \overline{T}_2^{(i)} - \beta/\overline{n}_{\mathrm{e}}^{(i)} \right)^2}{\left(\delta_{T_1}^{(i)} \right)^2 + \left(\alpha\, \delta_{T_2}^{(i)} \right)^2}, \qquad \text{(B.1)}$$

where $\delta_{T_{1,2}}$ represents the temperature map uncertainties, and β is set to zero when the regression is performed between T_{XMM} and T_{CXO}. The parameter space was sampled using Markov Chains, which we evolved according to the Metropolis-Hasting algorithm (Chib & Greenberg 1995), as done in Adam et al. (2015). We checked that this method correctly reproduced the true posterior likelihood using Monte Carlo realisations (pairs of temperature maps taken as the truth, to which we added a noise realisation as expected from the error estimates). Following (Pratt et al. 2009), we computed the overall scatter as

$$\sigma_{\mathrm{tot}}^2 = \frac{\frac{1}{N_{\mathrm{pix}}-2} \sum_i \frac{\left(k_{\mathrm{B}} \overline{T}_1^{(i)} - \alpha\, k_{\mathrm{B}} \overline{T}_2^{(i)} - \beta/\overline{n}_{\mathrm{e}}^{(i)} \right)^2}{\left(\delta_{T_1}^{(i)} \right)^2 + \left(\alpha\, \delta_{T_2}^{(i)} \right)^2}}{\frac{1}{N_{\mathrm{pix}}} \sum_i \frac{1}{\left(\delta_{T_1}^{(i)} \right)^2 + \left(\alpha\, \delta_{T_2}^{(i)} \right)^2}}, \qquad \text{(B.2)}$$

from which we extracted the intrinsic scatter, $\sigma_{\mathrm{int}} = \sqrt{\sigma_{\mathrm{tot}}^2 - \sigma_{\mathrm{stat}}^2}$, accounting for the statistical scatter σ_{stat}.

We also checked that our posterior likelihoods were consistent with the distribution of best-fitting values obtained when fitting independently our 100 Monte Carlo map realisations (T_{X} and T_{SZX}, see Appendix A and Section 3.4). Nevertheless, we stress that this fitting method does not fully account for the nature of the data themselves. Indeed the recovery of the X-ray spectroscopic temperature maps implies pixel-to-pixel correlations, which depend on the photon count statistics, and thus on the sky coordinate and cluster regions. The tSZ signal is also correlated in the NIKA data, but in a different way, due to beam effects, and the noise is spatially correlated. We thus expect that the T_{X} and T_{SZX} map pixels do not contain the exact same sky information. These complexities, inherent to the data, are not fully accounted for in our fit. This could lead to small displacements of the best-fit values that we recover, as well as a slight underestimation of the error contours. However, our baseline pixel size of 20 arcsec allows to mitigate these effects.